Optimal design of novel honeycomb photocatalytic reactors for numerical analysis of formaldehyde degradation by CFD modeling

Jinsen Gao
  Yancheng Institute of Technology

Pengyu Dong（✉ dongpy11@gmail.com ）
  Yancheng Institute of Technology

Junjian Tan
  Yancheng Institute of Technology

Lihua Zhang
  Yancheng Institute of Technology

Cunxia Wang
  Yancheng Institute of Technology

Abstract

As an alternative to the investigation of photocatalysts, it is a potential approach to enhance the photocatalytic performance of the novel photocatalytic reactor by optimizing its geometric structure and reaction conditions. In this work, five different honeycomb photocatalytic reactors with a deflector and a porous airflow distribution plate were designed and a numerical simulation was performed based on computational fluid dynamics (CFD). The simulation results showed that a huge vortex appeared near the entrance of the original model and the velocity distribution inside the reactor was non-uniform, whereas these shortcomings could be effectively overcome when using the 45° deflector model (S-4) compared to the other models. Compared to S-1, the photocatalytic conversion rate of formaldehyde for S-4 was boosted by 7.29% at a flow velocity of 0.04 m s^{-1}. In addition, it was found that the photocatalytic conversion rate of formaldehyde increased from 55.45−94.73% when the velocity decreased from 0.04 to 0.01 m s^{-1}, and the photocatalytic removal rate of formaldehyde decreased from 94.73−70.05% as the relative humidity varied from 20−70%. Furthermore, when the irradiance increased from 45 to 265 mW cm^{-2}, the photocatalytic conversion rate of formaldehyde improved by 10.78%. Overall, this work contributes to the design of the novel honeycomb reactor to acquire the optimized construction of the photocatalytic reactor.

Introduction

Nowadays, terrible indoor air quality (IAQ) has become a vital issue owing to the use of a large number of decoration materials and indoor-related combustion processes, therefore more reliable technology is required to remove the contaminants from the indoor air [1−3]. Photocatalytic oxidation (PCO) has been considered one of the promising and effective techniques for improving IAQ [4]. On the one hand, much work so far has focused on the modification of photocatalytic materials [5−9]. On the other hand, considerable research efforts have been dedicated to exploiting various photocatalytic reactors [10, 11], since the structure of photocatalytic reactors not only determines the photocatalytic performance but also has an impact on the mass transfer characteristics.

To improve the interactions between pollutant-catalyst surface (mass transfer) and light-catalyst (photon transfer), researchers have been developing new types of photocatalytic reactors, such as fluidized bed photocatalytic reactors and immobilized photocatalytic reactors [12]. In previous studies, immobilized photocatalytic reactors were designed such as the annular reactor [13, 14], multi-tube photocatalytic reactor [15, 16], corrugated plate photocatalytic reactor [17, 18], honeycomb monolith reactor [19, 20], optical fiber monolith reactor [21, 22], flat plate photocatalytic reactor [23, 24], to make up for their inevitable shortage of fewer reaction areas. Compared to other types of immobilized photocatalytic reactors, honeycomb reactors are the most prominent because of their large reaction area and low-pressure drop [25]. As a result, it is commonly employed in photocatalytic VOC degradation. Computational fluid dynamics (CFD) simulation is often employed as an effective measure to optimize the structure of the photocatalytic reactor, by which various chemical reactions and physical fields could be accurately simulated [26, 27]. For the different types of immobilized photocatalytic reactors, the CFD

model has been proposed to assess the performance of photocatalytic reactors under different physical fields, which can accurately predict the performance of photocatalytic reactors under diverse realistic operating conditions. The performance of the photocatalytic reactor can be improved by the following two methods: 1) increasing the reaction area and prolonging the residence time of pollutants in the reactor [28, 29]; 2) using different arrangements of light sources to improve the light radiation intensity [30, 31].

The previous investigations of the honeycomb reactors mainly focused on the light distribution, pressure, and velocity by simplifying the honeycomb into a porous media model to save computational time costs [32, 33]. However, the flow rate in each channel of the honeycomb reactor may be different, and the porous medium model could not reflect the specific details of the fluid field inside the reactor [34]. In consequence, the nature of the flow rate in each channel cannot be considered to be equal. The gas velocity affects the mass transfer characteristics and the photocatalytic performance of the reactor. Once the gas velocity of each channel was regarded as uniform, the simulation results would inevitably cause large errors.

In the present study, we investigate the flow in each channel of the honeycomb reactor to obtain the distribution of formaldehyde concentration instead of simplifying the honeycomb into a porous media model. According to the different configurations of the porous airflow distribution plate and deflectors, five kinds of honeycomb photocatalytic reactors with different structures were constructed to investigate their photocatalytic performance. The flow field characteristics of the photocatalytic reactors were investigated by analyzing the velocity vector and formaldehyde concentration distribution, and the optimal structural design of the photocatalytic reactor was finally determined. Moreover, the influences of radiation intensity and relative humidity on photocatalytic performance were discussed over the optimal reactor structure. Overall, this work provides some inspiration for designing photocatalytic reactors with outstanding transport performance and uniform airflow distribution properties.

Model Description

Geometrical model

To assess the photocatalytic performance for the removal of formaldehyde in the different reactors, a simplified structural model was employed for numerical simulation and analysis, as illustrated in Fig. 1a. The geometrical dimensions of the designed honeycomb photocatalytic reactor and the arrangement of the UV lamps were illustrated in Fig. S1 and Fig. S2 (in the Supplementary material), respectively. The central area was a honeycomb structure made of glass used as a catalyst carrier. The two end caps, consisting of the front chamber and the rear chamber, were fixed on both sides of the honeycomb. As a key component of the reactor, the honeycomb catalyst carrier was composed of 61 microchannels with a diameter of 15 mm along the circumference, as shown in Fig. 1b. The wall surfaces of these microchannels were coated with P25 TiO_2 powder catalyst for formaldehyde degradation reaction, and the porous inner wall of these microchannels could enhance the catalyst loading capacity. The overall

length and diameter of the honeycomb were 295 and 180 mm. The inlet and outlet diameters of the front chamber were set to 60 and 180 mm, respectively, and the distance between the inlet and the outlet was set to 90 mm. S-1 represented the original photocatalytic reactor. Based on the original model, the front chamber was constructed with four different designs. In the front chamber, S-2 denoted the installation of two layers of the porous airflow distribution plate. The distance between the first layer of the porous airflow distribution plate and the entrance was 30 mm, and 170 tiny holes with a diameter of 5 mm were uniformly distributed on the plate. The distance between the second layer of the porous airflow distribution plate and the entrance was 60 mm, and 310 tiny holes with a diameter of 5 mm were evenly distributed on the plate. Based on the structural design of S-2, the deflectors were also presented in the designs of S-3, S-4, and S-5, whereas the angle of deflectors was 40° for S-3, 45° for S-4, and 50° for S-5. The three view drawings of S-4 are shown in Fig. S3.

Flow field

The commercial software ANSYS/FLUENT 2020R2 was used to perform CFD simulations of the airflow and formaldehyde concentration distribution in the honeycomb photocatalytic reactors. The model was constructed in SpaceClaim to extract fluid fields. The fluid domain was loaded into ANSYS Fluent Meshing for mesh generation. The wall layer was encrypted to guarantee the accurate prediction of the surface mass transfer phenomenon at the core fluid field because the catalyst was mostly distributed on the wall surface. At the same time, the center of the first mesh layer closest to the wall surface ought to be placed at a non-dimensional distance (wall unit) of $y^+ < 1$, to achieve the specific details of airflow and formaldehyde concentration distribution at the viscous sublayer [35]. As illustrated in Fig. 2, the fluid domain is meshed by hexahedral core grids, which reduces the number of meshes while ensuring the accuracy of numerical simulation. At the same time, the boundary layer was added to the surface of the attached photocatalyst, and the number of the boundary layers was set to 5. The boundary layer grids grew from these surfaces in a ratio of 1.15 with the first grid layer having a thickness of 0.027 mm.

The airflow in the reactor could be regarded as turbulent according to its velocity. Due to the low flow rate of formaldehyde in the reactor, the low Reynolds number-type $k-\varepsilon$ model (Abe-Kondoh-Nagano model) was adopted [36–38] Compared to other low Reynolds number models, the AKN model could better predict the viscous sublayer flow and formaldehyde concentration distribution near the wall surface [39, 40]. The governing equations for the AKN model are given as follows [28]:

$$\frac{\partial \bar{U}_j}{\partial x_j} = 0 \# (1)$$

$$\frac{\partial \bar{U}_i}{\partial t} + \bar{U}_j \bullet \frac{\partial \bar{U}_i}{\partial x_j} = -\frac{1}{\rho} \bullet \frac{\partial \bar{P}}{x_i} + v\frac{\partial}{\partial x_j}\left(\frac{\partial \bar{U}_i}{\partial x_j} + \frac{\partial \bar{U}_j}{\partial x_i}\right) - \frac{\partial}{\partial x_j} \overline{u'_i u'_j} \# (2)$$

$$-\overline{u'_i u'_j} = v_t \left(\frac{\partial \bar{U}_i}{\partial x_j} + \frac{\partial \bar{U}_j}{\partial x_i}\right) - \frac{2}{3}k\delta_{ij} \# (3)$$

$$v_t = C_\mu \bullet f_\mu \bullet \frac{k^2}{\epsilon} \# (4)$$

$$\frac{\partial k}{\partial t} + \bar{U}_j \bullet \frac{\partial k}{\partial x_j} = D_k + P_k - \left(\bar{\epsilon} + D \right) \# (5)$$

$$\frac{\partial \bar{\epsilon}}{\partial t} + \bar{U}_j \bullet \frac{\partial \bar{\epsilon}}{\partial x_j} = D_\epsilon + \frac{\bar{\epsilon}}{k} \bullet \left(C_{\epsilon 1} \bullet P_k - C_{\epsilon 2} \bullet f_1 \bullet \bar{\epsilon} \right) + E \# (6)$$

where $\bar{U}_i$ (m s^{-1}) represents the ensemble-mean velocity, v_t (m^2 s^{-2}) signals the turbulent eddy viscosity, and k and ε denote the turbulent kinetic energy and its dissipation rate, respectively; f_μ and f_1 are the model functions of the $k-\varepsilon$ model with a low Reynolds number, which can be represented as:

$$f_\mu = \left\{ 1 - \exp\left(-\frac{y^*}{14} \right) \right\}^2 \left[1 + \frac{5}{R_t^{\frac{3}{4}}} \bullet exp\left\{ \left(\frac{R_t}{200} \right)^2 \right\} \right] \# (7)$$

$$f_1 = \left\{ 1 - \exp\left(-\frac{y^*}{3.1} \right) \right\}^2 \left[1 - 0.3 \bullet exp\left\{ -\left(\frac{R_t}{6.5} \right)^2 \right\} \right] \# (8)$$

$$R_t = \frac{k^2}{v\epsilon} \# (9)$$

$$y^* = \frac{u_\epsilon y}{v} = \frac{y}{\eta} \# (10)$$

$$\eta = \frac{v^{\frac{3}{4}}}{\epsilon^{\frac{1}{4}}} \# (11)$$

$$u_\epsilon = (v\epsilon)^{\frac{1}{4}} \# (12)$$

where R_t signals turbulent Reynolds number, y^* represents the nondimensional distance from the wall surface, η denotes the generalized coordinate in lower to upper wall direction, u_ϵ is the Kolmogorov velocity scale.

The Mach number represents the degree of compression of the gas in the flow. In this work, for the Mach number less than 0.3, the flow can be considered incompressible and simulated by using the pressure-based solver. Since the airflow in the reactor was incompressible, the governing equations were discretized by using the finite volume method (FVM) and the quadratic upstream interpolation for the convective kinetics (QUICK) scheme. The SIMPLE (semi-implicit method for pressure-link equations) algorithm was employed for the pressure and velocity coupling.

Formaldehyde transport equation and integration of reaction model

Assuming that the formaldehyde concentration at a certain point in the space is Y, the formaldehyde component transport model in the gas of the reactor is expressed by Eq. (13) [41].

$$\frac{\partial}{\partial t}(\rho Y) + \nabla \bullet \left(\rho \overrightarrow{v} Y\right) = -\nabla \bullet \overrightarrow{J} + S_{CH_2O} \# (13)$$

where S_{CH_2O} denotes the source term of formaldehyde due to the chemical reaction. $\overrightarrow{J}$ signals the diffusion flux of formaldehyde and is represented as Eq. (14):

$$\overrightarrow{J} = -\rho D \nabla Y \# (14)$$

where D denotes the molecular diffusion coefficient of formaldehyde in the gas phase. In this simulation, D is 2.88×10^{-5} m^2 s^{-1}.

The kinetic model of photocatalytic oxidation is currently described as the bimolecular or unimolecular type of the Langmuir-Hinshelwood (L-H) model. Since the mechanism of photocatalytic oxidation includes plenty of reaction pathways and steps, as well as a lot of reaction intermediates, exploiting a valid reaction rate model that is suitable for a wide range of pollutants and environments is a challenging task. Kinetic experiments were used to investigate the relationship between degradation rate and influencing factors.

In this work, considering the influence of water vapor on the purification efficiency of a photocatalytic reactor, a bimolecular type of the L-H kinetic model was employed to predict the flow field in the photocatalytic reactor. This bimolecular model was used to successfully correct the photocatalytic reaction rate of formaldehyde in the honeycomb reactor, as follows in Eq. (15) [32].

$$-r = K_0 \left(\frac{I}{I_G}\right)^n \frac{K_1 C_F}{1 + K_1 C_F + K_2 C_w} \frac{K_4 C_W}{1 + K_3 C_F + K_4 C_w} \# (15)$$

where K_0 denotes the rate constant with a value of 1.05 μmol cm^{-2} h^{-1}; I signals the incident radiation intensity in the honeycomb; K_1, K_2, K_3, K_4 represent the Langmuir adsorption equilibrium constants and their values are 1.02, 0.0002, 1.11, and 0.015 ppm^{-1}, respectively; C_W and C_F denote the concentrations of the water vapor and the formaldehyde, respectively.

Boundary conditions

The boundary conditions for the calculation domain of the photocatalytic reactor were set as follows. The inlet velocity and outlet pressure were set as the inlet and outlet boundary conditions, and the outlet pressure was set to 101325 Pa. The inlet velocity was along the x-direction and the inlet velocity was 0 in the y and z-directions. The ambient temperature was set to 298 K. The wall was set to a no-slip boundary condition, and the chemical reaction term was opened at the wall containing the P25 TiO$_2$ photocatalyst. To ensure the accuracy of the calculation, the convergence indexes for the formaldehyde concentration and other momentum were set to 10^{-6}. When the residual species in the reactor reached steady, the whole calculation was completed.

Validation and quality control of CFD

Since formaldehyde was the dominating pollutant in this work, the photocatalytic conversion rate of formaldehyde is a significant indicator to evaluate the photocatalytic reactor. The formaldehyde conversion rate X was calculated according to Eq. (16) [42].

$$X\ (\%) = \frac{C_{in} - C_{out}}{C_{in}} \times 100\% \# (16)$$

where C_{in} and C_{out} denote the formaldehyde concentration at the inlet and outlet, respectively. To achieve an appropriate grid number for simulation, a grid-independent study was conducted by analyzing the photocatalytic conversion rate of the formaldehyde and the formaldehyde concentration at the outlet for five different grid numbers from 0.75 to 4.32 million. As shown in Fig. 3, the photocatalytic conversion rate of the formaldehyde ascended with the increase of the grid number, but almost kept constant after the grid number exceeded 1.34 million. Thus, comprehensively taking into account calculation time and precision, the calculated grid number here was determined to be 1.34 million. With the above settings, the high prediction accuracy of the flow field and formaldehyde concentration in the honeycomb photocatalytic reactor was ensured.

Results And Discussion

Comparison and optimization of various designs

Figure 4 depicts the velocity vector for the five kinds of designed structural models of photocatalytic reactors in the X-Y plane at Z = 0.3 m. As shown in Fig. 4a, S-1 exhibits a large backflow vortex near the inlet, leading to partial formaldehyde gas cannot be discharged from the front chamber. With the airflow hitting the honeycomb constantly, a large vortex was generated [43]. Fewer vortices were presented at the inlet for the models of S-2, S-3, S-4, and S-5 compared with that for S-1, especially the vortex was absent at the inlet for S-4. Figure 4b illustrates the distribution of formaldehyde concentration in the center plane for these five models. It is observed that a lower concentration of formaldehyde was presented at the wall surface while a higher concentration appeared in the center of each hole of the honeycomb photocatalytic reactors, which might result from the fact that the P25 powder photocatalyst attached to the wall surface of the honeycomb hole. Moreover, the distribution of formaldehyde concentration was not uniform in S-1, where the formaldehyde concentration was much higher in the middle area compared with that on both sides of the honeycomb photocatalytic reactors in the X-Y plane. Compared to the S-1, the distribution of formaldehyde concentration for S-2, S-3, S-4, and S-5 was more uniform, and the best performance was presented in S-4. The improved distribution of formaldehyde concentration could be explained as follows. A porous airflow distribution plate could divide the airflow evenly into several fewer airflows, which reduced the airflow velocity and enhances the mass transfer [44, 45]. Moreover, the deflector could increase the residence time of formaldehyde in the photocatalytic reactor and thus improve the photocatalytic conversion rate of formaldehyde [46].

To deeply investigate the characteristics of formaldehyde concentration distribution for these different reactors, the velocity field in the reactors was performed. Figure 5 depicts the profiles of airflow velocity

for these five kinds of models. At a reaction gas flow rate of 0.04 m s^{-1}, the gas velocity declined significantly when the formaldehyde flowed into the honeycomb photocatalytic reactor through the inlet and boosted gradually when the gas approached the outlet. It is worth noting that S-1 showed a higher velocity in the middle region of each hole than that on its two sides. Compared to S-1, the other honeycomb photocatalytic reactors of S-2, S-3, S-4, and S-5 exhibited a more uniform velocity distribution, especially S-4 showed a favorable uniform performance for the flow velocity.

As shown in Fig. 6a, the maximum pressure of S-1 is presented at the entrance of the honeycomb, while the pressure of other models (S-2, S-3, S-4, and S-5) is mainly concentrated at the porous airflow distribution plate and deflectors. As illustrated in Fig. 6b, the S-4 exhibits the maximum pressure, while the original model (S-1) displays relatively lower pressure. This is because the airflow was unobstructed in the front chamber of the S-1 and hit the honeycomb directly, leading to a large pressure on the honeycomb. On the contrary, the presence of a porous airflow distribution plate and deflectors in the front chamber of other models (S-2, S-3, S-4, and S-5) could make airflow change the direction of flow, which results in the maximum pressure at these positions.

Effects of flow velocity

To analyze the effects of the inlet velocity on the photocatalytic conversion rate of formaldehyde, the velocity was set to 0.01, 0.015, 0.02, 0.03, and 0.04 m s^{-1}, respectively. The distribution of formaldehyde concentration at various flow velocities for S-4 is depicted in Fig. S4. Figure 7a illustrates the photocatalytic conversion rate of formaldehyde for these five kinds of reactors under different flow rates, while other conditions are kept constant. It is obvious that S-4 exhibited the highest photocatalytic conversion rate of formaldehyde among these reactors despite various flow rates. Meanwhile, compared to S-1, when the inlet velocity ranged from 0.01 to 0.04 m s^{-1}, the photocatalytic conversion rate of formaldehyde for the S-4 was increased by 3.2% for 0.01 m s^{-1}, 3.96% for 0.015 m s^{-1}, 4.91% for 0.02 m s^{-1}, 6.52% for 0.03 m s^{-1}, and 7.92% for 0.04 m s^{-1}, respectively. It is noted that the improvement magnitude of the photocatalytic conversion rate of formaldehyde for S-4 relative to S-1 boosted gradually with the increase of the inlet velocity, resulting from the shortened contact time between the formaldehyde molecules and photocatalyst layer at a higher velocity of the fluid, which made it difficult to be adsorbed and degraded [47]. When the inlet velocity decreased, the formaldehyde concentration became lower and lower at the outlet region and reached the lowest value at 0.01 m s^{-1}. It might be due to the low airflow velocity, which kept formaldehyde staying longer in the reactor, leading to a more complete reaction [21]. As illustrated in Fig. 7b, the formaldehyde concentration for S-4 decreases with reducing the flow velocity. It can be observed that the formaldehyde concentration at the outlet region varied from 727.6 to 86.1 ppb when the inlet velocity ranged from 0.04 to 0.01 m s^{-1}, approximately decreasing by 8.5 times. The results show that the formaldehyde concentration is almost proportional to reaction time and inversely proportional to the airflow velocity.

Effects of relative humidity on PCO performance

In general, water molecules have both positive and negative effects on the photocatalytic reaction. On the one hand, increasing humidity is conducive to improving photocatalytic oxidation efficiency. On the other hand, there is a competitive adsorption relationship between water molecules and formaldehyde molecules, which reduces the performance of photocatalytic oxidation [20]. Therefore, the effects of relative humidity on formaldehyde concentration and PCO in the best reactor of S-4 were investigated by altering the relative humidity (RH) in the range of 20−70%, when the radiation intensity (116 mW cm^{-2}) and inlet velocity (0.01 m s^{-1}) were kept constant. Figure 8 displays the distribution of formaldehyde in the center plane (Z = 0.3 m) with relative humidity ranging from 20−70%. As the relative humidity increased from 20−70%, the photocatalytic conversion rate of formaldehyde decreased from 94.73−70.05%, a reduction of approximately 24.68%. It means the photocatalytic reaction rate of formaldehyde depends on the humidity level, and the worst photocatalytic performance was presented when the relative humidity was at 70%. At the same time, an approximately linear relationship was observed between the relative humidity and the photocatalytic conversion rate of formaldehyde, as shown in Fig. 9a. The formaldehyde concentration at the outlet region of the photocatalytic reactor boosted from 94 ppb to 509 ppb when relative humidity increased from 20−70%. The corresponding distribution of formaldehyde concentration at various cross-sectional planes along the x-direction for S-4 is shown in Fig. S5. As illustrated in Fig. 9b, the formaldehyde concentration was constant at the front and the end of the reactor, whereas the formaldehyde concentration in the honeycomb varied significantly under different relative humidity levels. When the relative humidity is varied from 20−70%, water molecules mainly compete with formaldehyde to adsorb, which leads to a reduction in the photocatalytic conversion rate of formaldehyde [35, 48].

Influences of radiation intensity on PCO performance

It is generally considered that the increase in radiation intensity results in the production of much more photoinduced electron-hole pairs, corresponding to an increase in hydroxyl radical (·OH) generation and formaldehyde degradation rates. Radiation intensity varied from 45 to 265 mW cm^{-2} when analyzing the influences of radiation intensity on PCO and formaldehyde concentration in the optimized photocatalytic reactor of S-4, while the relative humidity (20%) and inlet velocity (0.01 m s^{-1}) were kept constant. The distribution of formaldehyde concentration to radiation intensity is illustrated in Fig. 10. The formaldehyde concentration at the outlet region of the photocatalytic reactor decreased from 226 ppb to 37 ppb when radiation intensity increased from 45 to 265 mW cm^{-2}. Figure 11a presents the relationship between the photocatalytic conversion rate of formaldehyde and radiation intensity. It is found that the formaldehyde conversion rate boosted when the radiation intensity increased. As the radiation intensity increased from 45 to 116 mW cm^{-2}, the photocatalytic conversion rate of formaldehyde was boosted by 7.61%. However, the formaldehyde conversion rate increased slowly when the radiation intensity exceeded 116 mW cm^{-2}. With the radiation intensity increased from 116 to 265 mW cm^{-2}, the formaldehyde conversion rate improved by only 3.17%. As illustrated in Fig. 11b, the formaldehyde concentration for S-4 decreases at various monitoring points with the increase of radiation intensity. A possible explanation is depicted as follows. The irradiation exponential factor *n* of the kinetic reaction

rate is 1 (first order) at low radiation intensity, where the photocatalytic reaction is dominant compared with the recombination of photoinduced electron-hole pairs; and n is 0.5 (half-order) at high radiation intensity, where recombination rate of photoinduced charge is the main factor in comparison with photocatalytic chemical reaction [49, 50]. Herein, the relationship between the photocatalytic reaction rate and light intensity can be described as a half-order relationship since radiation intensity varies from 45 to 265 mW cm^{-2} in this work.

Conclusion

In this work, a novel honeycomb photocatalytic reactor with a deflector of 40°, 45°, and 50°, and a porous airflow distribution plate for formaldehyde degradation was designed based on the CFD simulation, which significantly improved the uneven airflow distribution and enhanced the photocatalytic performance for formaldehyde removal. The simulation results showed that S-4 had the best photocatalytic performance. The influences of velocity, relative humidity, and irradiation intensity on the photocatalytic conversion rate of formaldehyde were numerically simulated in detail. Results show that the photocatalytic conversion rate of formaldehyde raised from 55.45–94.73% when the inlet flow velocity decreased from 0.04 to 0.01 m s^{-1}. Moreover, the photocatalytic conversion rate of formaldehyde decreased from 94.73–70.05% when the relative humidity varied from 20–70%. Furthermore, with the irradiation intensity increased from 45 to 265 mW cm^{-2}, the photocatalytic conversion rate of formaldehyde was boosted by 10.78%. Compared with the original model (S-1), the optimal designed S-4 significantly improved the photocatalytic conversion rate of formaldehyde by 7.29% at a flow rate of 0.04 m s^{-1}. Overall, this work made it easier to design this extremely effective photocatalytic reactor, which effectively improves the photocatalytic formaldehyde removal rate.

Declarations

Availability of data and materials The data used to support the findings of this study are available from the corresponding author upon request.

References

1. M.N. Anwar, M. Shabbir, E. Tahir, M. Iftikhar, H. Saif, A. Tahir, M.A. Murtaza, M.F. Khokhar, M. Rehan, M. Aghbashlo, M. Tabatabaei, A.-S. Nizami, J. Hazard. Mater. **416**, 125851 (2021)

2. A.H. Goldstein, W.W. Nazaroff, C.J. Weschler, J. Williams, Environ. Sci. Technol. **55**, 100 (2021)

3. T. Salthammer, S. Mentese, R. Marutzky, Chem. Rev. **110**, 2536 (2010)

4. M. Schreck, M. Niederberger, Chem. Mater. **31**, 597 (2019)

5. R. Bensouilah, L. Olivet, T. Hammedi, S. Pronier, J. Barbier, C. Fontaine, A. Ghorbel, Z. Ksibi, Res. Chem. Intermed. **47**, 813 (2021)

6. F. Salvadores, O.M. Alfano, M.M. Ballari, Appl. Catal., B **268**, 118694 (2020)

7. M. Salami, A. Ezabadi, Res. Chem. Intermed. **45**, 3673 (2019)

8. S. Weon, F. He, W. Choi, Environ. Sci. Nano. **6**, 3185 (2019)

9. J. Howeizi, S. Taghvaei-Ganjali, M. Malekzadeh, F. Motiee, S. Sahebdelfar, Res. Chem. Intermed. **45**, 3165 (2019)

10. M. Le Bechec, N. Costarramone, T. Pigot, S. Lacombe, Chem. Eng. Technol. **39**, 26 (2016)

11. Y. Boyjoo, H. Sun, J. Liu, V.K. Pareek, S. Wang, Chem. Eng. J. **310**, 537 (2017)

12. Q. Geng, Q. Wang, Y. Zhang, L. Wang, H. Wang, Res. Chem. Intermed. **39**, 1711 (2013)

13. Y. Qin, Z. Wang, J. Jiang, L. Xing, K. Wu, Chem. Eng. J. **394**, 124917 (2020)

14. F. Khodadadian, M.W. de Boer, A. Poursaeidesfahani, J.R. van Ommen, A.I. Stankiewicz, R. Lakerveld, Chem. Eng. J. **333**, 456 (2018)

15. J. Roegiers, J. van Walsem, S. Denys, Chem. Eng. J. **338**, 287 (2018)

16. J. van Walsem, J. Roegiers, B. Modde, S. Lenaerts, S. Denys, Chem. Eng. J. **354**, 1042 (2018)

17. Y.M. Jiao, A.T. Kovala, H. Shang, J.A. Scott, Can. J. Chem. Eng. **97**, 1760 (2019)

18. C. Passalía, O.M. Alfano, R.J. Brandi, Ind. Eng. Chem. Res. **50**, 9077 (2011)

19. M. Tahir, B. Tahir, Appl. Surf. Sci. **377**, 244 (2016)

20. K.-P. Yu, W.-M.G. Lee, G.-Y. Lin, Aerosol Air Qual. Res. **15**, 1008 (2015)

21. K. Yuan, L. Yang, X. Du, Y. Yang, Energy Convers. Manage. **87**, 258 (2014)

22. H. Chen, F. Chu, L. Yang, O. Ola, X. Du, Y. Yang, Appl. Energy **230**, 1403 (2018)

23. S.W. Verbruggen, S. Lenaerts, S. Denys, Chem. Eng. J. **262**, 1 (2015)

24. J.O.B. Lira, H.G. Riella, N. Padoin, C. Soares, Chem. Eng. Process. **154**, 107998 (2020)

25. S. Roy, T. Bauer, M. Al-Dahhan, P. Lehner, T. Turek, AlChE J. **50**, 2918 (2004)

26. O.B.L.J. de, N. Padoin, V.J.P. Vilar, C. Soares, J Hazard Mater **372**, 145 (2019)

27. Y. Boyjoo, M. Ang, V. Pareek, Chem. Eng. Sci. **111**, 266 (2014)

28. H. Einaga, J. Tokura, Y. Teraoka, K. Ito, Chem. Eng. J. **263**, 325 (2015)

29. F. Long, B. Deng, Y. Xu, J. Gao, Y. Zhang, J. Water Process Eng. **31**, 100824 (2019)

30. T. Claes, A. Dilissen, M.E. Leblebici, T. Van Gerven, Chem. Eng. J. **361**, 725 (2019)

31. C. Casado, R. Timmers, A. Sergejevs, C.T. Clarke, D.W.E. Allsopp, C.R. Bowen, R. van Grieken, J. Marugán, Chem. Eng. J. **327**, 1043 (2017)

32. X. Wang, X. Tan, T. Yu, Ind. Eng. Chem. Res. **53**, 18402 (2014)

33. T. Ming, H. Gui, T. Shi, H. Xiong, Y. Wu, Y. Shao, W. Li, X. Lu, R. de Richter, Sol. Energy **226**, 101 (2021)

34. K. Tong, L. Yang, X. Du, Chem. Eng. J. **400**, 125988 (2020)

35. K. Nakahara, M. Muttakin, K. Yamamoto, K. Ito, Indoor Built Environ. **29**, 163 (2019)

36. S.-Y. Wu, X.-Q. Yan, L. Xiao, Sol. Energy **199**, 460 (2020)

37. K. Abe, T. Kondoh, Y. Nagano, Int. J. Heat Mass Transfer **37**, 139 (1994)

38. K. Abe, T. Kondoh, Y. Nagano, Int. J. Heat Mass Transfer **38**, 1467 (1995)

39. J.E. Duran, M. Mohseni, F. Taghipour, Water Qual. Res. J. **50**, 21 (2014)

40. J. Esteban Duran, F. Taghipour, M. Mohseni, Int. J. Heat Mass Transfer **52**, 5390 (2009)

41. H. Luo, G. Zhang, Z. Hashisho, L. Zhong, Build. Simul. **13**, 1095 (2020)

42. X. Xie, C. Hao, Y. Huang, Z. Huang, Sci. Total Environ. **724**, 138059 (2020)

43. V. Muñoz, C. Casado, S. Suárez, B. Sánchez, J. Marugán, Catal. Today **326**, 82 (2019)

44. Y. Zhao, L. Yue, S. Wang, L. Li, F. Wang, Int. J. Heat Mass Transfer **127**, 55 (2018)

45. F. Dolati, N. Amanifard, H.M. Deylami, Energy **154**, 352 (2018)

46. J.S. Devia-Orjuela, L.A. Betancourt-Buitrago, F. Machuca-Martinez, Environ. Sci. Pollut. Res. Int. **26**, 4510 (2019)

47. S.-Y. Wu, L. Xu, L. Xiao, Renew. Energ. **148**, 338 (2020)

48. D. Kibanova, M. Sleiman, J. Cervini-Silva, H. Destaillats, J. Hazard. Mater. **211-212**, 233 (2012)

49. A.H. Mamaghani, F. Haghighat, C.-S. Lee, Appl. Catal., B **203**, 247 (2017)

50. M. Malayeri, F. Haghighat, C.-S. Lee, Build. Environ. **154**, 309 (2019)
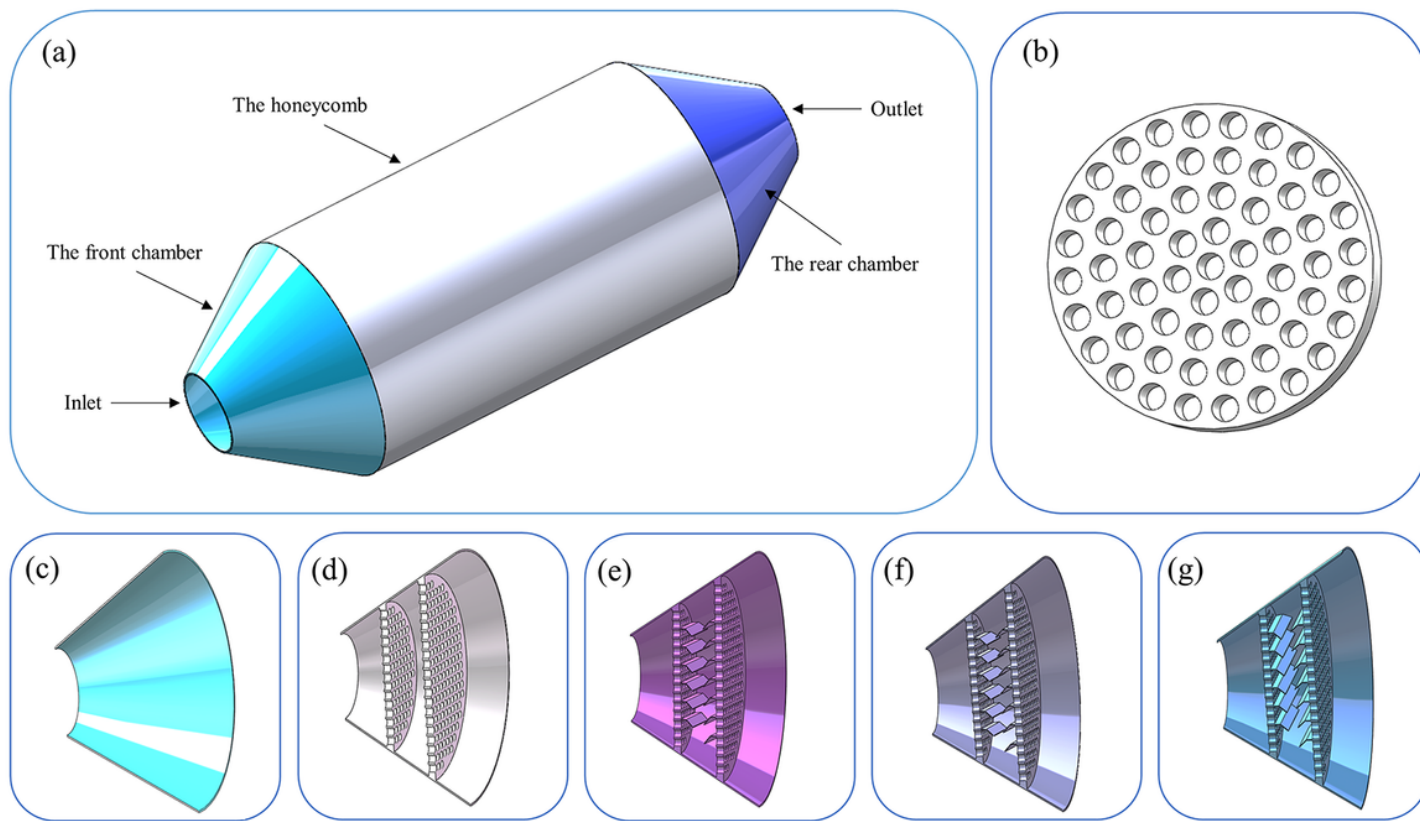
Figures

Figure 1

(a) The overall structure of the designed photocatalytic reactor, (b) the inside honeycomb structure, and various designs of the front chamber: (c) S-1, (d) S-2, (e)S-3, (f) S-4, and (g) S-5
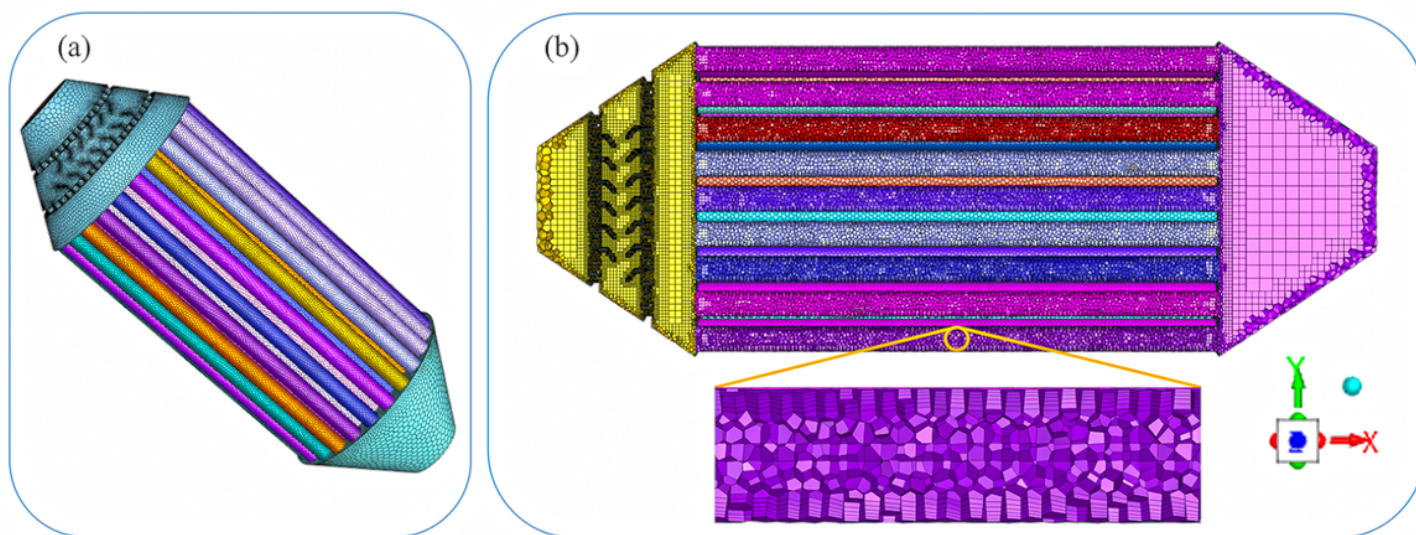

Figure 2

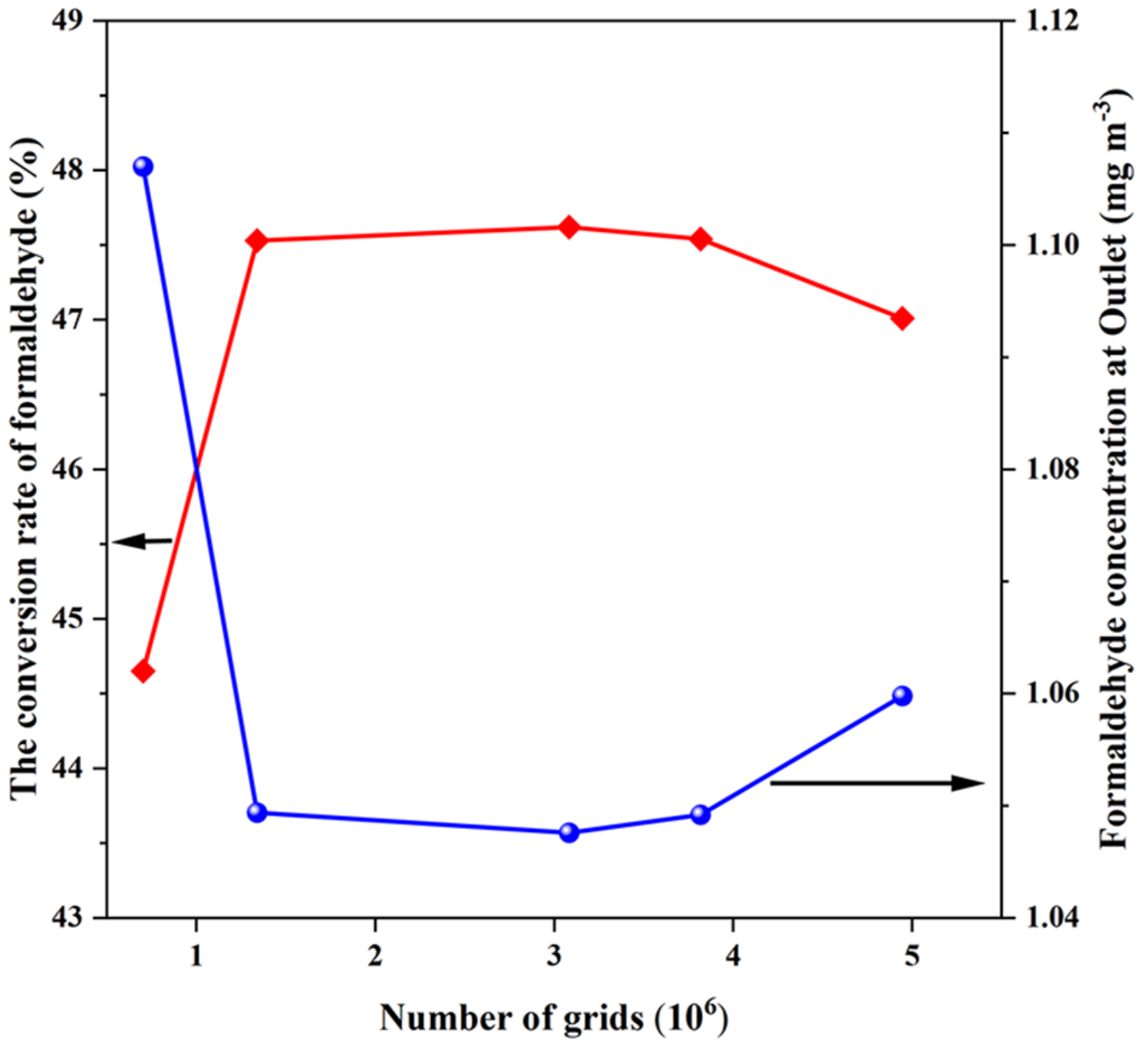(a) The grids of photocatalytic reactors, and (b) the grids on the x-y section and boundary layer grids

Figure 3

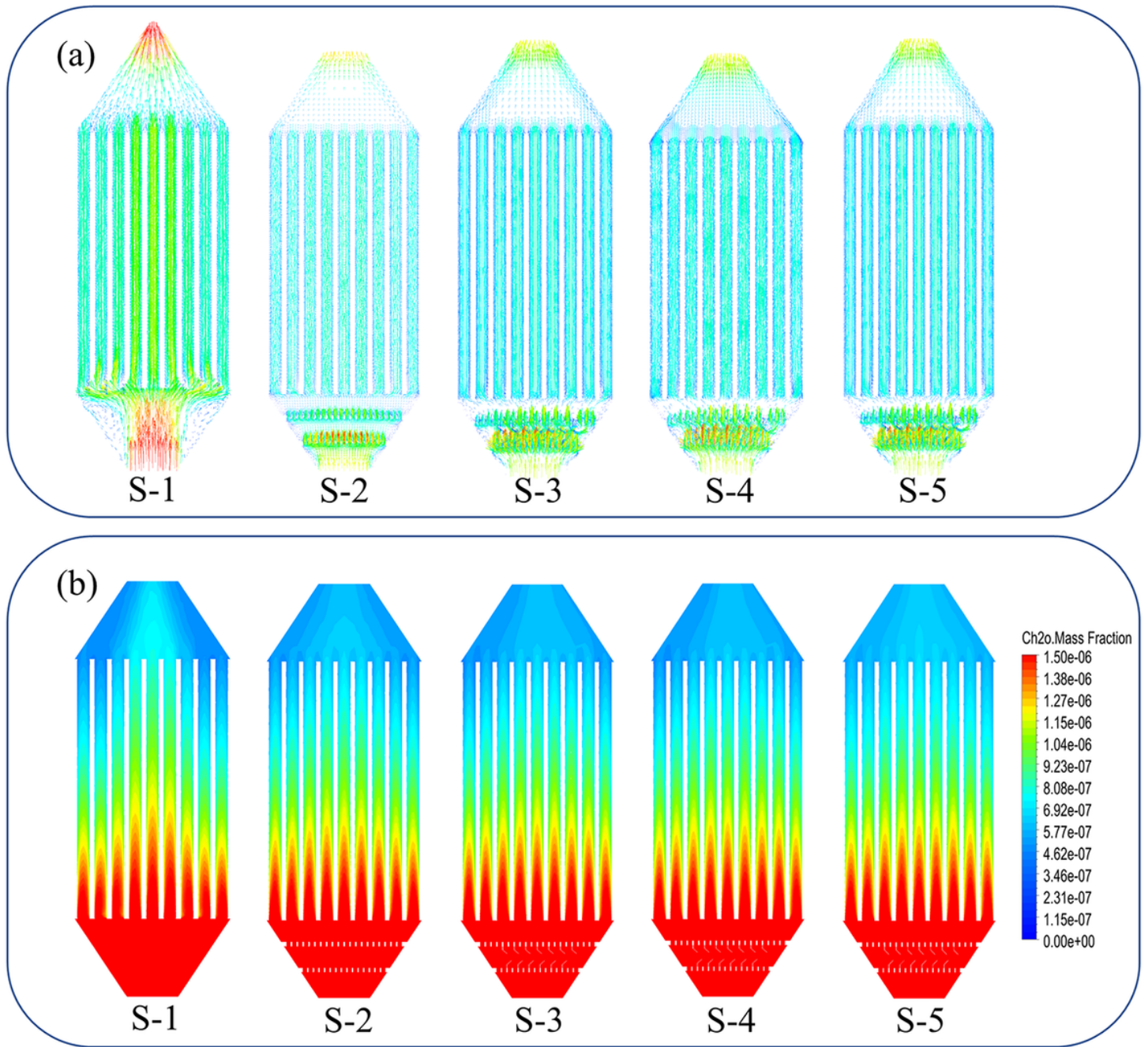Grid independence analysis for the photocatalytic conversion rate of formaldehyde and the corresponding formaldehyde concentration at the outlet

Figure 4

(a) The velocity vector for the different reactors and (b) the distribution of formaldehyde concentration for the different reactors
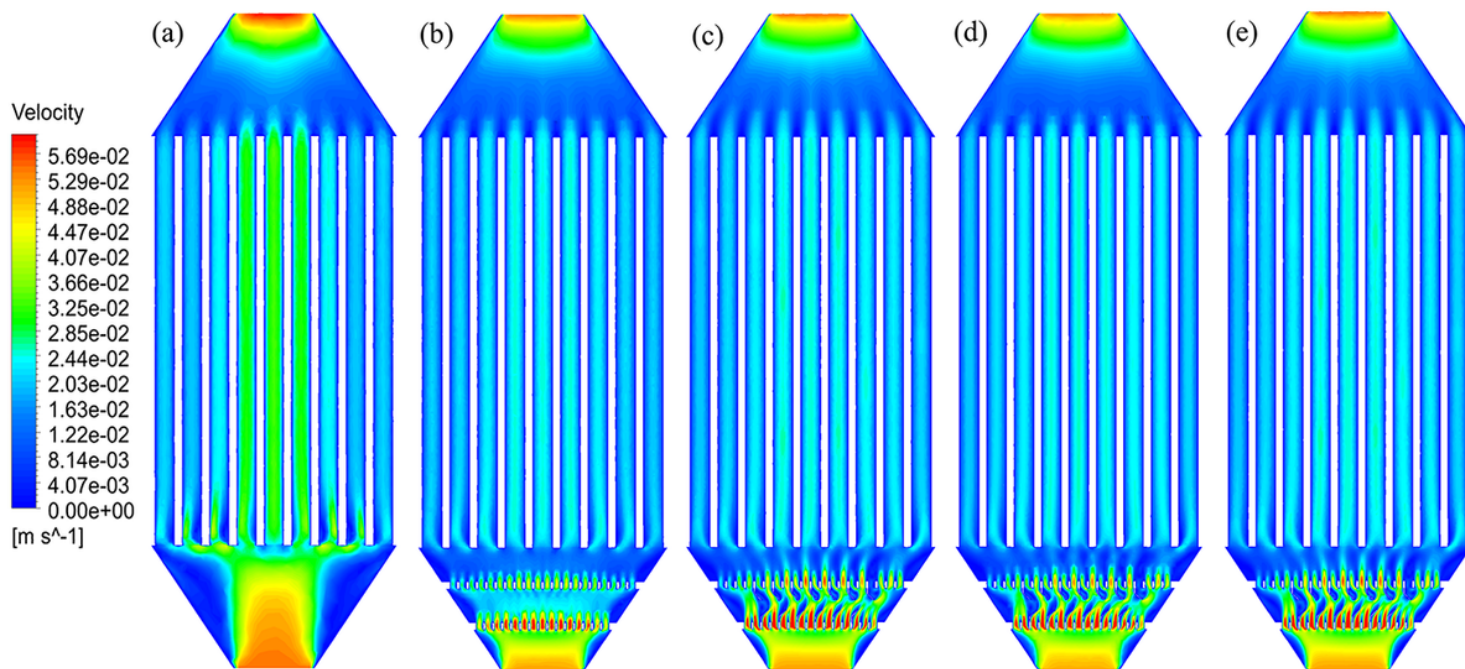
Figure 5

The distribution of velocity for the different reactors: **(a)** S-1, **(b)**S-2, **(c)** S-3, **(d)** S-4, and **(e)** S-5
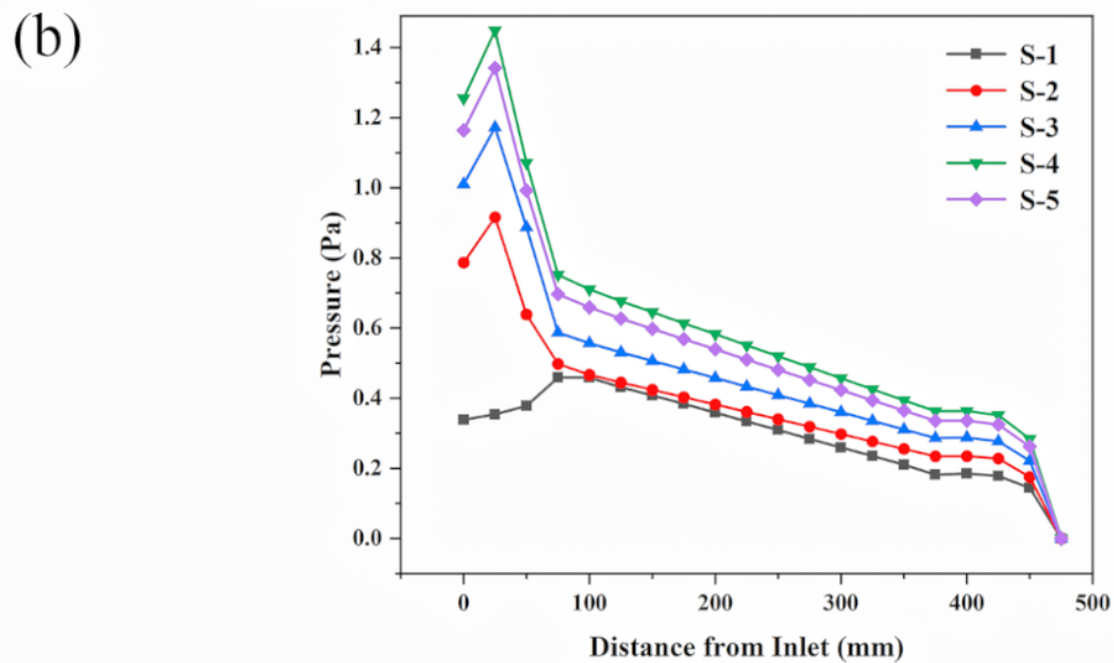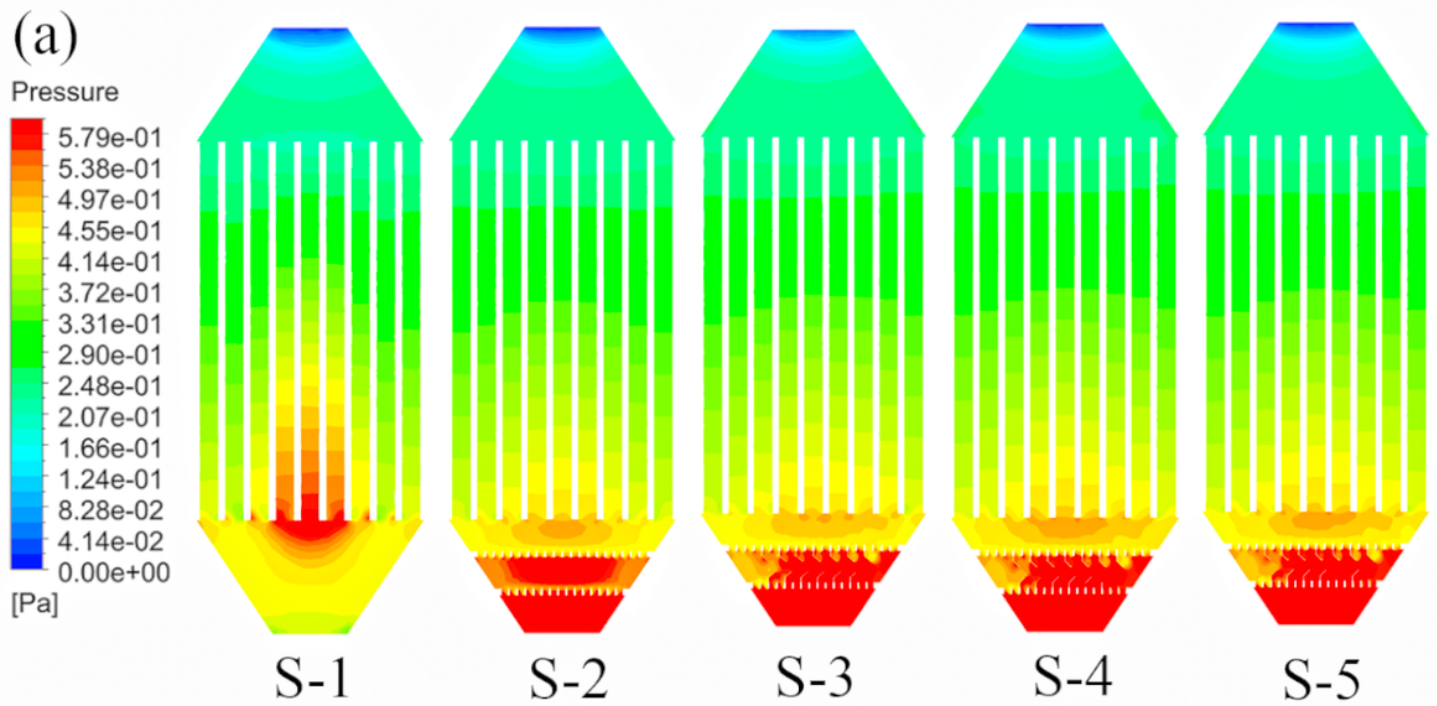
Figure 6

(a) Pressure distribution for different designs and (b) the pressure drop along x direction for different designs
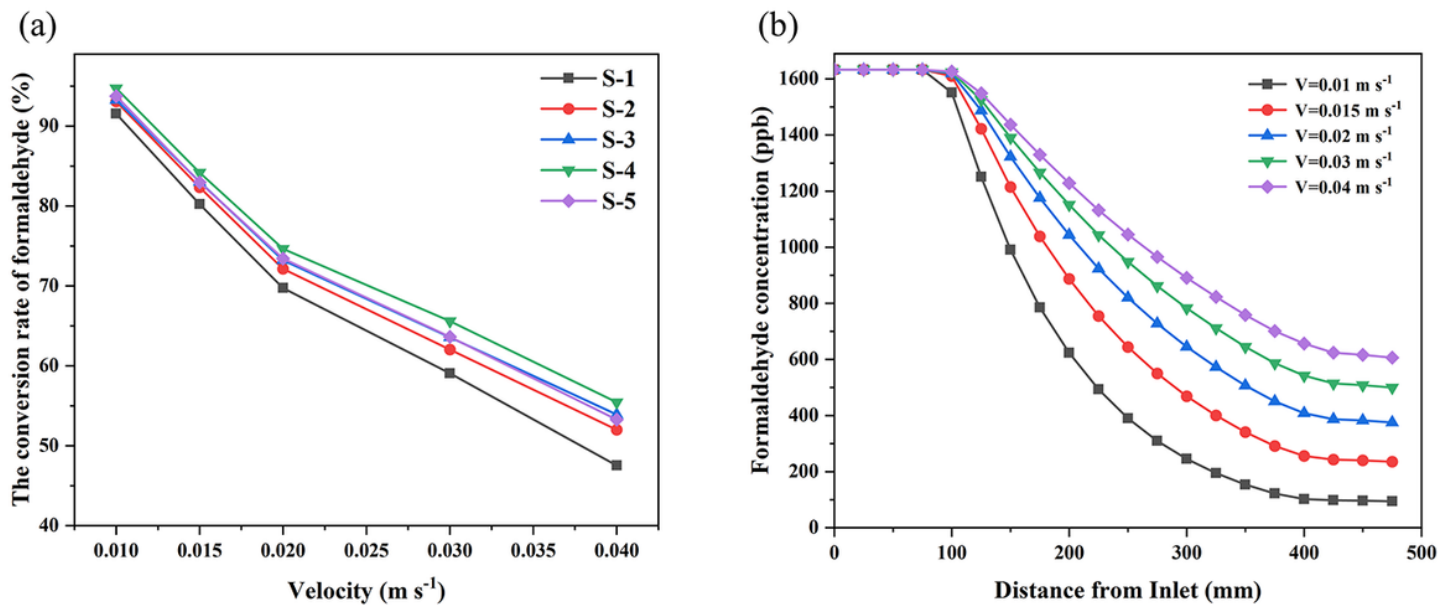
Figure 7

(a) The photocatalytic conversion rate of formaldehyde for five kinds of reactors under different flow rates and (b) the formaldehyde concentration distribution along x direction at various velocities for S-4
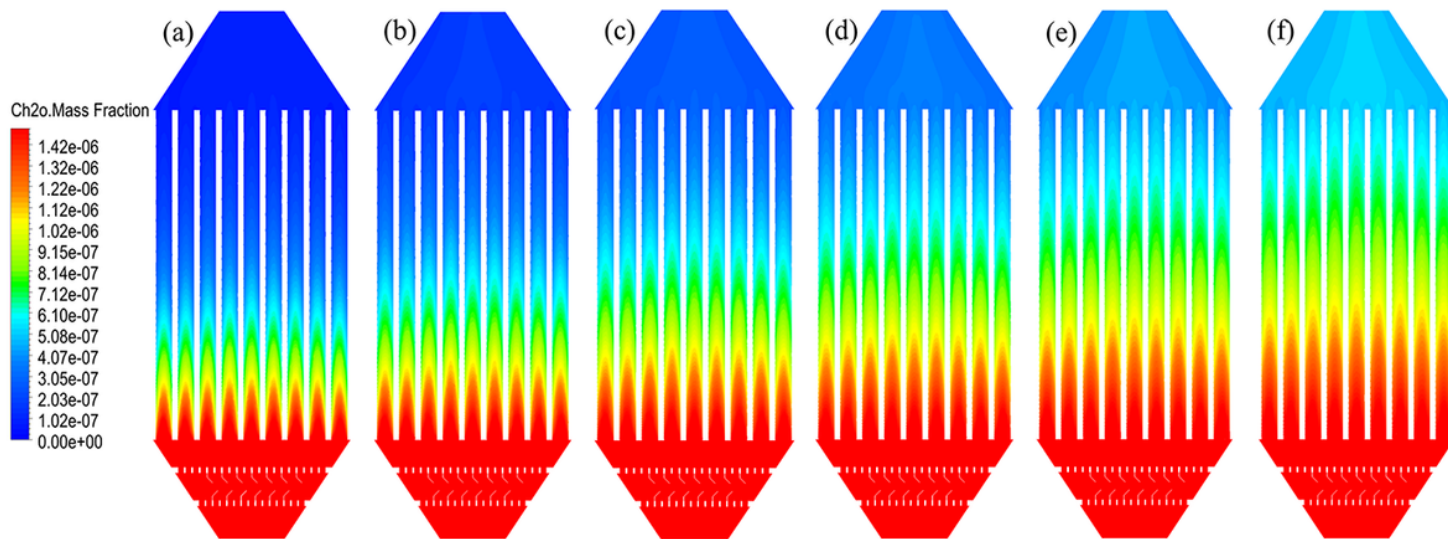

Figure 8

The distribution of formaldehyde concentration in relation to relative humidity for S-4: (a) 20%, (b) 30%, (c)40%, (d) 50%, (e) 60%, and (f) 70%
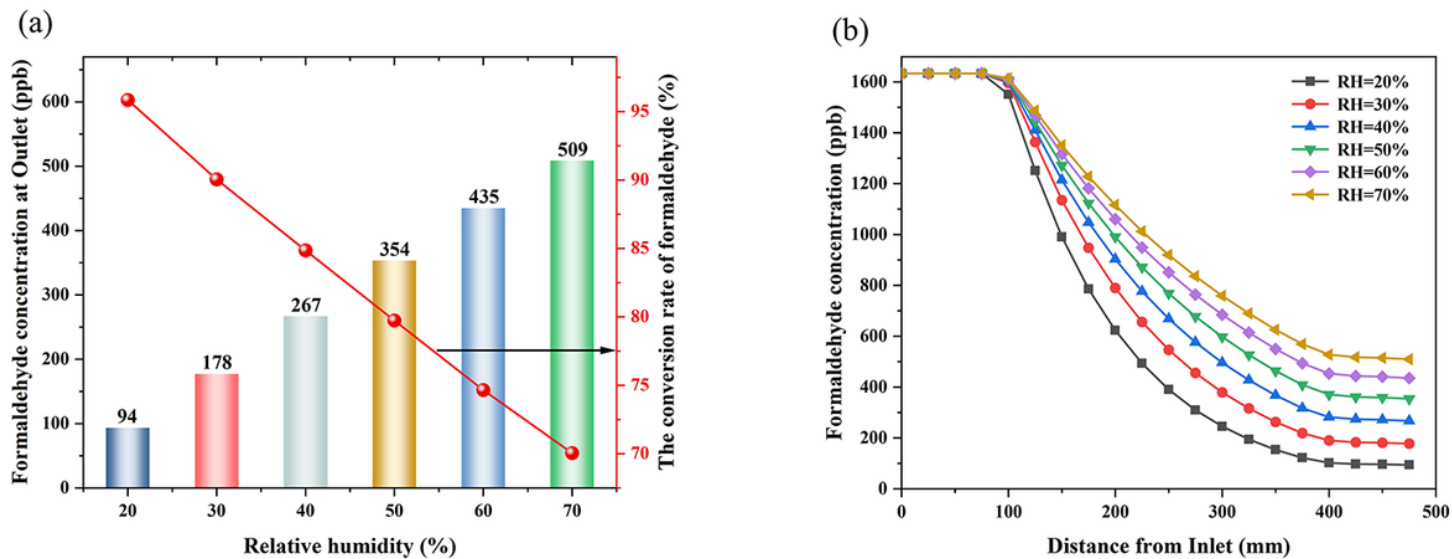
Figure 9

(a) Relationship between relative humidity and photocatalyticformaldehyde conversion rate, and (b) the formaldehyde concentration distribution along x direction at various relative humidity for S-4
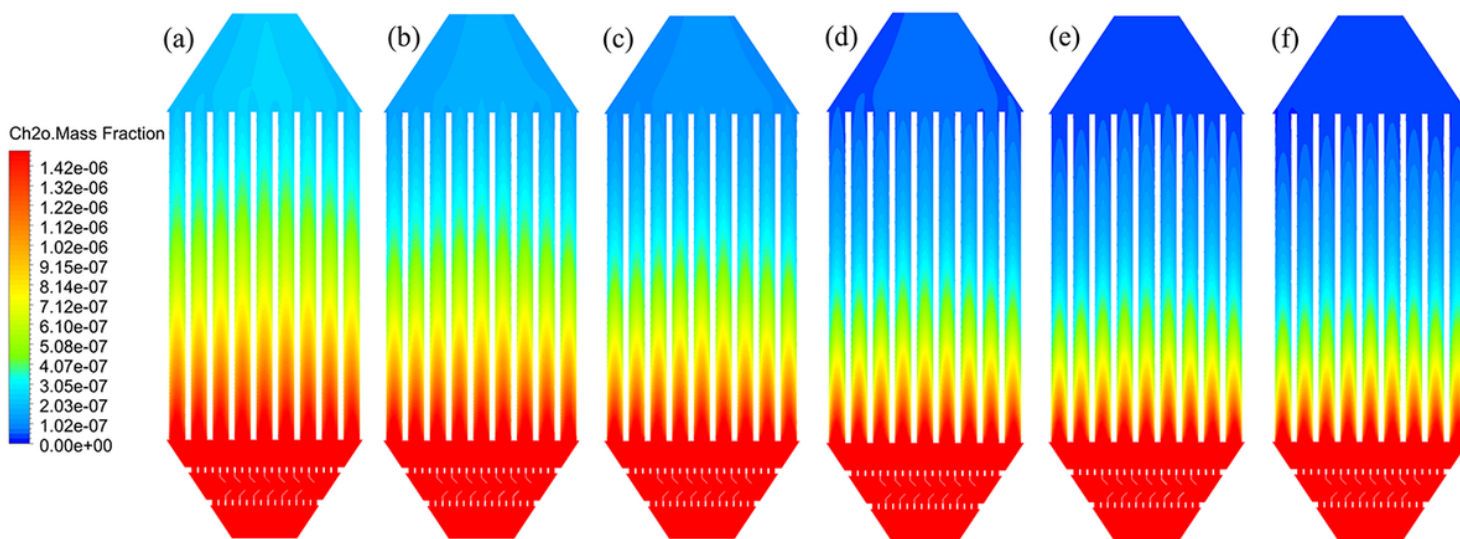

Figure 10

The distribution of formaldehyde concentration in relation to radiation intensity for S-4: (a) 45, (b) 65, (c) 96, (d) 175, (e) 225, and (f) 265 mW cm^{-2}
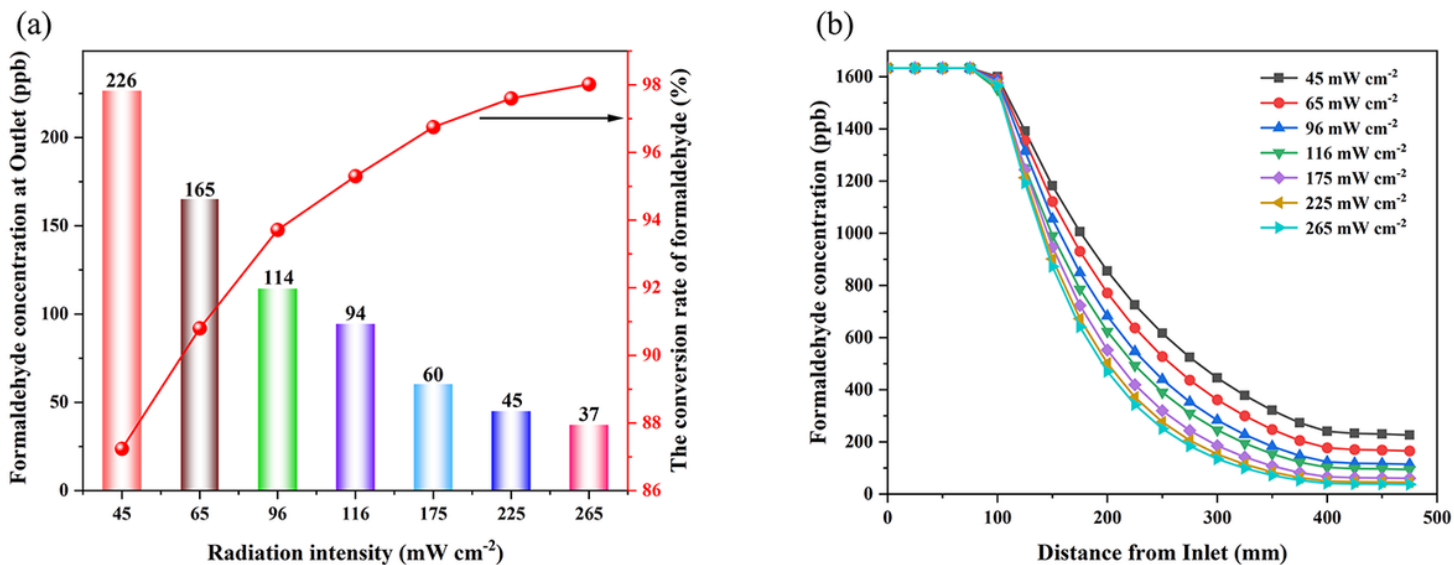
Figure 11

(a) Relationship between photocatalytic formaldehyde conversion rate and radiation intensity and **(b)** the formaldehyde concentration distribution along x direction at various radiation intensities for S-4

Supplementary Files

This is a list of supplementary files associated with this preprint. Click to download.

- SupplementaryInformation.docx